Li Metal Batteries

In Situ Formation of Bifunctional Interlayer on 3D Conductive Scaffold for Dendrite-Free Li Metal Batteries

Yonghwan Kim [iD], Dohyeong Kim [iD], Minjun Bae, Yujin Chang, Won Young An, Hwichan Hong, Seon Jae Hwang [iD], Dongwan Kim, Jeongyeon Lee* [iD], and Yuanzhe Piao* [iD]

Regulating lithium (Li) plating/stripping behavior in three-dimensional (3D) conductive scaffolds is critical to stabilizing Li metal batteries (LMBs). Surface protrusions and roughness in these scaffolds can induce uneven distributions of the electric fields and ionic concentrations, forming "hot spots." Hot spots may cause uncontrollable Li dendrites growth, presenting significant challenges to the cycle stability and safety of LMBs. To address these issues, we construct a Li ionic conductive-dielectric gradient bifunctional interlayer (ICDL) onto a 3D Li-injected graphene/carbon nanotube scaffold (LGCF) via in situ reaction of exfoliated hexagonal boron nitride (fhBN) and molten Li. Microscopic and spectroscopic analyses reveal that ICDL consists of fhBN-rich outer layer and inner layer enriched with Li_3N and Li-boron composites (Li-B). The outer layer utilizes dielectric properties to effectively homogenize the electric field, while the inner layer ensures high Li ion conductivity. Moreover, DFT calculations indicate that ICDL can effectively adsorb Li and decrease the Li diffusion barrier, promoting enhanced Li ion transport. The modulation of Li kinetics by ICDL increases the critical length of the Li nucleus, enabling suppression of Li dendrite growth. Attributing to these advantages, the ICDL-coated LGCF (ICDL@LGCF) demonstrates impressive long-term cycle performances in both symmetric cells and full cells.

1. Introduction

The growing demand for practical energy storage devices has led to significant advancements in the technology of lithium (Li) ion batteries (LiBs) to achieve superior power and energy densities. However, conventional LiBs, using graphite as anodes, with its low theoretical specific capacity ($372 \, mAh \, g^{-1}$), are unable to fulfill the high-power and energy density requirements of mobile electronics and electric vehicles (EVs).[1–3] Therefore, Li metal batteries (LMBs) employing Li metal as anodes, known for their low electrochemical potential (-3.04 V vs standard hydrogen electrode), notably low density ($0.534 \, g \, cm^{-3}$), and impressive high theoretical specific capacity ($3860 \, mAh \, g^{-1}$), are considered one of the most promising candidates for an anode.[4–7] Nevertheless, the commercialization of Li metal anodes (LMAs) is impeded by the following severe drawbacks: 1) uncontrollable formation of Li dendrites, leading to separator penetration and short circuits, critically undermines battery safety and stability,[8–10] 2) the infinite volume expansion during cycling leads to cracks on the solid electrolyte interphase (SEI) layer, and 3) an unstable Li/electrolyte interface.[11–13]

To address these challenges, several strategies have been employed, including the introduction of electrolyte additives,[14–19] solid electrolytes,[20–24] and three-dimensional (3D) conductive scaffolds for hosting Li metal, such as modified copper foam, carbon cloth, MXenes aerogel, and nickel foam to host Li metals.[25–31] The utilization of a 3D graphene/carbon nanotube scaffold (GCF) for hosting Li metal has been demonstrated as an effective way, owing to its ability to accommodate volume changes and facilitate uniform Li ion flux distribution. Additionally, its mechanical durability and large electroactive surface area contribute significantly to stabilizing LMBs.[32,33] Furthermore, the lithiophilic functional groups (such as C-OH and C-OOH) of GCF facilitate not only the molten Li injection into GCF but also the formation of Li-carbon composites (Li-C) known for their lithiophilicity and high electron conductivity.[34,35] However, as fabricated Li-injected GCF (LGCF) presents localized electric field polarization due to surface protrusions and roughness. These localized electron accumulations at the interface between electrode and electrolyte cause uneven Li ion distribution, resulting in "hot-spots" with intensified local electric fields, which exacerbate uneven Li nucleation and growth.[36] In this regard, achieving the uniformly distributed electric field to minimize Li ion concentration gradient is crucial to achieving homogeneous Li deposition.[37]

Electric field modulation can be achieved by adopting an electronically insulating interlayer with high dielectric constant materials. The

Y. Kim, D. Kim, M. Bae, Y. Chang, W. Y. An, H. Hong, S. J. Hwang, D. Kim, Dr. Y. Piao
Department of Applied Bioengineering, Graduate School of Convergence Science and Technology, Seoul National University, Suwon-si, Gyeonggi-do 16229, Korea
E-mail: parkat9@snu.ac.kr
J. Lee
School of Fashion and Textiles, The Hong Kong Polytechnic University, Hung Hom, Kowloon, Hong Kong SAR, China
E-mail: httpower@snu.ac.kr
Dr. Y. Piao
Advanced Institutes of Convergence Technology, Suwon-si, Gyeonggi-do 16229, Korea
[iD] The ORCID identification number(s) for the author(s) of this article can be found under https://doi.org/10.1002/eem2.12861.

high dielectric materials can guide electrons and ions towards negative and positive poles, respectively. This movement of electrons and ions generates an electric dipole layer at the interface between the electrode and the electrolyte, homogenizing the distribution of the electric field as well as the Li ion concentration.[38,39] Previous studies have successfully applied high dielectric materials such as paraffin wax (PW), barium titanate (BTO), and poly(vinylidene fluoride-co-hexafluoropropylene) (PVDF-HFP) as interfacial layers, effectively alleviating the irregularity of electrons/Li ion concentrations by redistributing Li ion flux.[40–42] Despite such advantages, an additional dielectric layer on the 3D conductive scaffold can inevitably enlarge voltage polarizations due to extended Li ion diffusion length, leading to the premature reach of the cut-off voltage during cycling and thereby resulting in reduced capacities.[40] Therefore, when designing a functional layer on a 3D conductive scaffold, Li ion conductivity as well as Li diffusion kinetics must be put into consideration.

Herein, we in situ introduce a Li ionic conductive-dielectric gradient bifunctional interlayer (ICDL) onto LGCF (ICDL@LGCF) to stabilize Li-hosted 3D conductive scaffold and enhance the operation of LMBs. The ICDL is composed of exfoliated hexagonal boron nitride (fhBN) rich outer layer and Li_3N and Li-boron composites (Li-B) rich inner layer. The innovative ICDL@LGCF design for LMBs shows multiple advantages: 1) The fhBN-rich outer layer of ICDL has dielectric properties that serve to homogenize the electric field distribution, effectively reducing the gradient of Li ion concentration at the interface between the electrode and the electrolyte.[43] Additionally, the Lewis acidic B atoms in fhBN interact with Lewis basic Li ions to improve Li ion flux;[44,45] 2) The Li_3N and Li-B rich inner layer of ICDL enhances Li ion conductivity and facilitates rapid diffusion of Li ions across the whole electrode, thereby avoiding the accumulation of Li at the electrode surface;[46,47] 3) the 3D LGCF conductive scaffold serving as the Li host mitigates severe volume expansions during cycling. Based on the synergistic combination effects of ICDL@LGCF, highly reversible Li plating/stripping behaviors are observed by ex situ scanning electron microscopy (SEM) analysis. Additionally, density functional theory (DFT) provides further evidence that ICDL is advantageous for the adsorption of Li and accelerating Li ions transport. Furthermore, classical nucleation theory confirms from a thermodynamic standpoint that ICDL effectively inhibits the Li dendrite's growth. Consequently, ICDL@LGCF symmetric cell demonstrates remarkable cycling stability of 1600 h at $1\,mA\,cm^{-2}$ with a $1\,mAh\,cm^{-2}$. Furthermore, full cells paired with $LiFePO_4$ (LFP) exhibit good cycle stability and a considerable capacity retention of 93.4% after 300 cycles at 1 C. When paired with $LiNi_{0.8}Co_{0.1}Mn_{0.1}O_2$ (NCM811) cathode, ICDL@LGCF full cells demonstrate a better cycle stability compared with bare Li over 200 cycles.

2. Results and Discussion

We selected fhBN as the source for the ICDL due to its distinct advantages over traditional interlayer materials such as barium titanate (BTO) and polymer-based materials such as PVDF-HFP. Although BTO offers a high dielectric constant, its heavy density ($6.0\,g\,cm^{-3}$) is a drawback for battery applications.[41] Similarly, polymer-based materials are susceptible to phase changes from temperature fluctuations and generally require ceramic additives to achieve sufficient insulating properties, adding complexity to their use.[40,48,49] In contrast, fhBN is lightweight ($2.09\,g\,cm^{-3}$), chemically stable, and mechanically durable, maintaining structural integrity during repeated Li plating/stripping cycles.[44]

Additionally, fhBN reacts thermodynamically with molten Li to form Li_3N and Li-B, both of which exhibit high Li ion conductivity.[50,51] This eliminates the need for extra ceramic additives, thus preserving power density and improving battery stability.[48,52] Therefore, we propose a one-step process in which fhBN reacts with molten Li to form the ICDL, integrating it directly onto the LGCF framework. For the control material, we synthesized LGCF without an ICDL to directly observe the synergetic effects of ICDL as a dielectric property and Li ion conductivity through electrochemical methods and theoretical calculation.

The ICDL@LGCF was fabricated by a facile step-by-step vacuum filtration and molten Li injection process as shown in **Figure 1**a. First, a 20 mL aqueous solution of graphene oxide (GO) and carbon nanotube (CNT) mixture (2:1 wt %) was mixed using ultra-sonication to form a GO/CNT solution. In addition, a 2 mL aqueous solution ($1\,mg\,mL^{-1}$) of fhBN was also prepared. Second, a step-by-step vacuum filtration method was employed to synthesize fhBN-coated GO/CNT scaffold (fhBN@GOCF) by sequentially pouring 1) GO/CNT solution and 2) fhBN solution. The obtained fhBN@GOCF hydrogel was freeze-dried for 2 days. Third, the fhBN@GOCF was introduced into the glove box and brought into contact on a hot plate at 300 °C. A spark reaction occurred simultaneously with the reduction reaction of GO, leading to the formation of fhBN@GCF. In Figure 1b,c, the scanning electron microscopy (SEM) images show the top surface and cross-sectional morphologies of fhBN@GCF. The fhBN nanoflakes, with a lateral size of 50–100 nm, were distributed across the top surface of fhBN@GCF. While the optical digital image in Figure 1b shows a light gray color indicative of fhBN coverage, the SEM image revealed some areas where the coverage may be incomplete, suggesting the formation of nanoscale voids between the flakes. These nanoscale voids, however, could allow for faster Li-ion diffusion and enhance interfacial dynamics, potentially leading to improved electrochemical performance. The thickness of fhBN@GCF was approximately ∼270 μm. In Figure S1a,b, Supporting Information, the fhBN region of the cross-sectional SEM image shows that the thickness of fhBN layer was approximately ∼3 μm, with fhBN nanoflakes uniformly covering the surface. Meanwhile, in the GCF region, the CNTs were uniformly anchored on the graphene sheets, providing improved electron conductivity.[53] In addition, CNTs prevented the dense staking of graphene sheets during filtration and derived the interlayer porous structure, indicating a 3D scaffold for providing enough space for Li plating. In Figure 1d, energy dispersive X-ray spectroscopy equipped with SEM (SEM-EDS) image further confirms that fhBN layer uniformly covered the top surface of GCF, where N and B elements from fhBN were strongly detected with uniform distribution on the top surface, while the C element from GCF was detected in the overall structure. Without the addition of fhBN solution during vacuum filtration, the GCF was also prepared. In Figure S2a–d, Supporting Information, the SEM images show the top and cross-sectional morphologies of GCF. The graphene and CNT composites were observed on the top surface of GCF without fhBN flakes, and the thickness of GCF was measured at approximately ∼250 μm with a uniform dispersion of C and O elements (Figure S3, Supporting Information). In Figure 1e, X-ray diffraction (XRD) reveals that fhBN@GCF exhibited a peak at 42.6°, attributed to the fhBN layer. In addition, both fhBN@GCF and GCF displayed a typical broad peak at 26°, indicating the reduction of GO during the spark reaction.[54] The X-ray photon spectroscopy (XPS) was performed to reveal the elemental compositions of fhBN@GCF. In Figure 1f,g, the high-resolution N 1s and B 1s spectra confirm the presence of fhBN on the surface of GCF. The peaks at 399.1 eV for N 1s and 191 eV for B 1s correspond to the B-N bond in
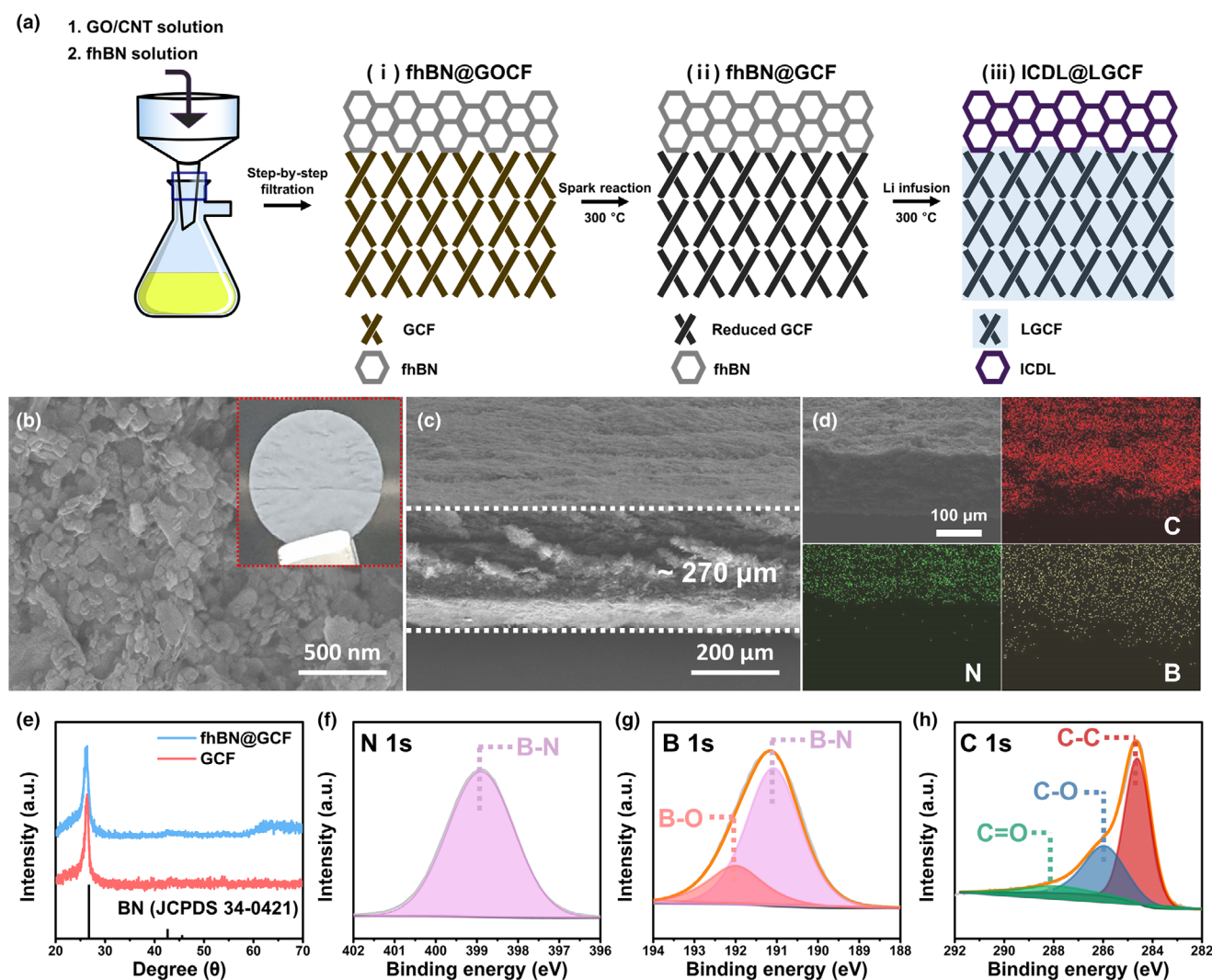
Figure 1. a) Schematic illustration of the synthesis process of fhBN@GCF and ICDL@LGCF. b) Top-view and c) cross-sectional SEM images of fhBN@GCF. The inset in b) is the optical image of fhBN@GCF. d) Cross-sectional SEM-EDS mapping of fhBN@GCF. e) XRD patterns of fhBN@GCF and GCF. High-resolution f) N 1s, g) B 1s, and h) C 1s XPS spectra of fhBN@GCF.

fhBN.[55] Meanwhile, the peak at 192 eV for B 1s corresponded to the B-O bond in fhBN.[55,56] The peak shift of 0.8 eV both in N 1s and B 1s, compared to fhBN@GOCF was observed due to the oxygen decoupling during the heating process (Figure S4, Supporting Information).[57,58] The high-resolution spectrum of C 1s showed three distinct peaks located at 284.8, 286.5, and 288.3 eV, which correspond to C-C, C-O, and C=O bonds, respectively (Figure 1h).[59]

In the final synthesis process, the fhBN@GCF was immersed in molten Li. The lithiophilic oxygen functional groups and the spaces between the pores and gaps of the GCF allowed the molten Li to easily fill the spaces within the scaffold and simultaneously react with the GCF, resulting in the in situ formation of Li-carbon composites (Li-C).[60] Furthermore, the fhBN layer was converted into Li_3N and Li-boron composites (Li-B) during the molten Li injection process. The synthesized Li_3N and Li-B provided high Li ionic conductivity and a low Li diffusion barrier, favoring the kinetics of the LMAs, while the residual unreacted fhBN preserved its dielectric properties.

Consequently, the newly designed layer, consisting of Li_3N, Li-B, and fhBN, was designated as the ICDL.

To investigate the morphology and thickness of ICDL@LGCF, SEM analysis was performed. As shown in **Figure 2a**, the ICDL underwent a color transition from light gray to dark-purple, indicating the conversion of fhBN into Li_3N and Li-B components. The surface of LGCF maintained a similar morphology to that described in Figure 1b,c, with flake-shaped nanoparticles of the ICDL distributed across the surface. They were well-dispersed and interconnected with each other to form conductive networks. The thickness of ICDL was approximately 3 μm, as depicted in Figure 2b. The formation of dense ICDL with a homogeneous distribution of N and B elements on the surface of ICDL@LGCF was further supported by SEM-EDS analysis as shown in Figure S5, Supporting Information. The compact ICDL was expected to protect the underlying Li metal from reactions with the electrolyte and inhibit Li dendrite growth, as confirmed by the atomic force microscopy (AFM) surface morphology results shown in Figure S6a, Supporting
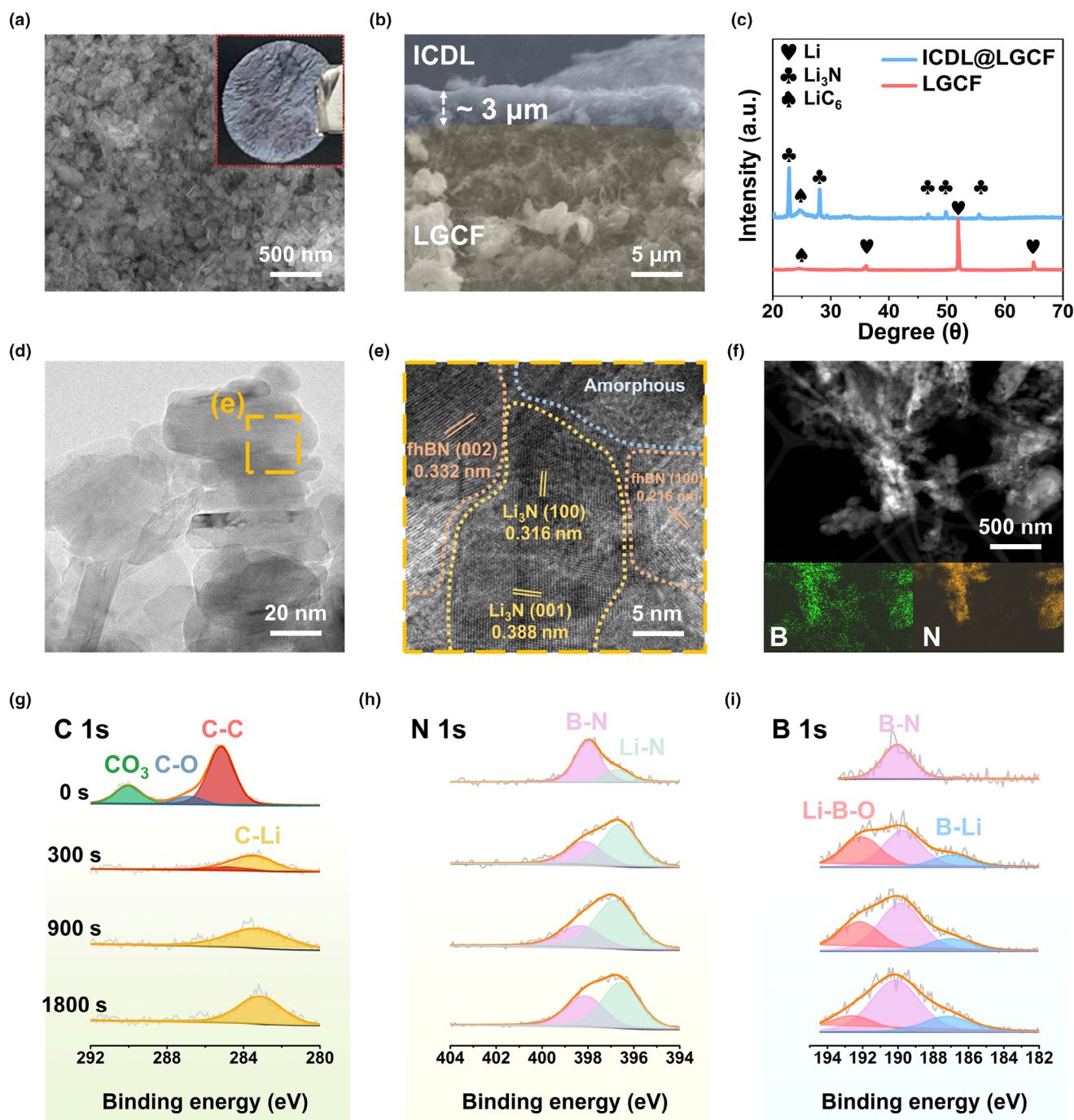
Figure 2. a) Top-view and b) cross-sectional SEM images of ICDL@LGCF. c) XRD patterns of ICDL@LGCF and LGCF. d) TEM and e) HRTEM images of ICDL. f) EDS mappings of ICDL. XPS depth profile of g) C 1s, h) N 1s, and i) B 1s of ICDL@LGCF.

Information. The ICDL@LGCF surface exhibited a smooth and flat morphology. In contrast, the LGCF displayed a different surface morphology (Figures S6b and S7, Supporting Information), with Li metal and Li-C covering the top surface, resulting in island-like protrusions and a higher average surface roughness (R_a) (154.5 nm) compared to ICDL@LGCF (110.4 nm). The higher average surface roughness of LGCF can lead to localized electric fields and hot-spot regions, which

promote Li dendrite formation and electrolyte decomposition. In comparison, the lower surface roughness of ICDL@LGCF can contribute to a more uniform and homogeneous Li plating/stripping process.

In cross-sectional SEM images, Li was uniformly infused into the pores and gaps of both ICDL@LGCF and LGCF, resulting in a densely packed Li host structure (Figure S8, Supporting Information). Following molten Li injection, the thicknesses of ICDL@LGCF and LGCF

slightly increased from 270 to 275 μm and 250 to 290 μm, respectively, suggesting the mechanical stability of the 3D LGCF scaffold for hosting Li and its potential to mitigate volume expansion during Li plating/stripping. Figure S9, Supporting Information, shows that the areal capacity of ICDL@LGCF was measured to be approximately 32 mAh cm^{-2}, corresponding to a specific capacity of 3360 mAh g^{-1} (calculated based on the electrode weight), achieving 87% of the theoretical capacity of Li metal. Additionally, the thickness of the ICDL@LGCF could be controlled by varying the volume of the GO/CNT solution during the synthesis process, ranging from 180 to 320 μm. The corresponding areal capacities for different thicknesses of ICDL@LGCF were measured to be 24–39 mAh cm^{-2}.

To further investigate the chemical compositions and structure of ICDL, additional material characterizations were conducted. As shown in Figure 2c, the ICDL@LGCF was composed of crystalline Li$_3$N- and Li-C-related components by XRD analysis. The five distinct peaks located at 22.9, 28.0, 46.5, 49.8, and 55.3°, corresponding to Li$_3$N, with a broad peak at 24.6°, attributed to LiC$_6$.[50,61] Surprisingly, no Li peaks were detected, indicating crystalline Li$_3$N covered the ICDL@LGCF, suggesting potential improvements in Li ionic conductivity. Although residual fhBN was not detectable through XRD, its presence was confirmed using HRTEM and XPS, which are discussed in a subsequent section. On the other hand, LGCF showed a broad peak at 24.6° of LiC$_6$ and three distinct peaks at 36, 52, and 64.9° which were attributed to Li.[60] This indicated that metallic Li was exposed on the surface of LGCF, and such a direct exposure of Li metal to electrolyte directly could lead to side reactions and growth of Li dendrites. The morphology and composition of the ICDL were further analyzed using high-resolution transmission electron microscopy (HRTEM) equipped with EDS analysis. The ICDL was scraped from ICDL@LGCF for HRTEM characterization. As illustrated in Figure 2d, the flake-shaped frameworks of fhBN were preserved even after molten Li infusion, which was similar to fhBN scraped from the fhBN@GCF as shown in Figure S10, Supporting Information. The coexistence of multiple components and various grains was observed by HRTEM images and fast Fourier transform (FFT) patterns of ICDL (Figure 2e and Figure S11, Supporting Information). The crystalline components with lattice spacings of 0.388, 0.316, 0.216, and 0.332 nm, which correspond to Li$_3$N (001), Li$_3$N (100), fhBN (100), and fhBN (002) planes, respectively, were observed. The amorphous region of ICDL might contain mixed components of Li, B, and N elements together. Moreover, the HRTEM-EDS mapping image (Figure 2f) also demonstrated a uniform distribution of N and B elements originating from fhBN, Li$_3$N, and Li-B. This suggested that during the Li infusion process, reactions occurred between fhBN and Li atoms within the framework, leading to a hybrid layer where multiple components were integrated within the fhBN. This grain-boundary-rich structure composed of multiple high Li ion conductive materials is expected to provide fast Li ion diffusion channels.[62]

To gain a deeper understanding of the spatial compositions and structure of the ICDL, the high-resolution depth-dependent XPS analysis with Ar$^+$ sputtering was conducted as illustrated in Figure 2g–i. The XPS spectra of C 1s in Figure 2g present that the ICDL exhibited three distinct peaks at 284.8, 286.8, and 290.0 eV attributing to C-C, C-O, and C=O species, respectively, before Ar$^+$ etching.[63] Upon subsequent etching from 300 to 1800 s, the above three peaks disappeared, while the new peak corresponding to Li-C species (283.3 eV) showed a gradual increase from the surface to the interior of ICDL.[59,60] The emergence of Li-C in the internal region could be attributed to

the LGCF component. The high electronic conductivity provided by Li-C facilitated superior electron channels at the interface between ICDL and LGCF.[64] From the high-resolution XPS spectra of N 1s (Figure 2h), the two peaks at 396.7 and 398.1 eV, corresponding to Li$_3$N and fhBN, were observed on the outer surface of ICDL.[50,63] Interestingly, the contents of Li$_3$N became prominent after the etching process, while the signal of fhBN species still existed without obvious change. In the B 1s XPS spectra, the signal at 190.1 eV was assigned to fhBN before Ar$^+$ etching. After the subsequent etching process, The emergence of peaks at 187.2 and 192.1 eV, corresponding to B-Li and Li-B-O bonds within the interior of ICDL, confirms the presence of Li-B components.[47,65] Similar with N 1s spectra, the fhBN species still existed in the overall structure of ICDL. Based on the XPS depth results, the spatial components and structure of the ICDL were characterized by a bifunctional interlayer, with both Li ionic conductivity and dielectric properties gradually distributed within the interlayer. The outer layer, rich in fhBN, served a dielectric property, distributing the electric field uniformly and homogenizing Li ion flux to effectively minimize the gradient of Li ion concentration at the Li metal/electrolyte interface.[66] Conversely, the inner layer of the ICDL was predominantly composed of Li$_3$N and Li-B, enhancing Li ionic conductivity and providing a low Li diffusion barrier. Furthermore, beneath the ICDL, the presence of Li-C provided excellent electron pathways, potentially serving as sites where Li ions and electrons could be evenly distributed. To verify the homogeneous electric field distribution enabled by the dielectric properties of the fhBN in the ICDL, we conducted Kelvin probe force microscopy (KPFM) measurements. The surface electrical potential obtained from KPFM allowed us to calculate the work function values for each electrode.[67,68] As shown in Figure S12, Supporting Information, the average work function of ICDL@LGCF was found to be 2.13 eV, compared to 1.46 eV for LGCF. The higher work function of ICDL@LGCF was attributed to the dielectric properties of fhBN-rich outer layer in the ICDL. This indicated that the ICDL layer effectively prevents electrons from penetrating through the ICDL and reacting with the electrolyte, thereby inhibiting unwanted side reactions.[67] Furthermore, the distribution of work function values was more uniform in ICDL@LGCF compared to LGCF, suggesting that the ICDL layer effectively modulated the electric field. Overall, these results suggested that the ICDL could promote homogeneous transport of Li ions and electrons at the interface between the ICDL and LGCF during Li plating/stripping processes.

To investigate the surface morphology changes of ICDL@LGCF, LGCF, and bare Li after cycling tests, we disassembled the symmetric cells after 100 cycles at the current density of 1 mA cm^{-2} with a capacity of 1 mAh cm^{-2}. The morphologies of the electrodes were characterized by ex-situ SEM analysis. **Figure 3a** compares top-view SEM images of bare Li, LGCF, and ICDL@LGCF. As shown in SEM images, the surfaces of bare Li and LGCF became rough with a porous structure, featuring numerous Li dendrites. The porous structure of Li dendrites increased the surface area and led to side reactions with electrolytes.[9,17] In contrast, the surface of ICDL@LGCF was maintained flat and densely packed without any Li dendrites. In addition, cross-sectional SEM images highlighted the significant effect of ICDL as shown in Figure 3b. Numerous Li dendrites needles (highlighted by red circles) were observed on the surface of bare Li and LGCF, taking a risk of short circuit. However, no Li dendrites were observed on the surface of ICDL@LGCF, which maintained a flat and compact dense surface. Further investigation into the electrode structure during the Li stripping/plating process at 1 mA cm^{-2}, with various Li capacities, was
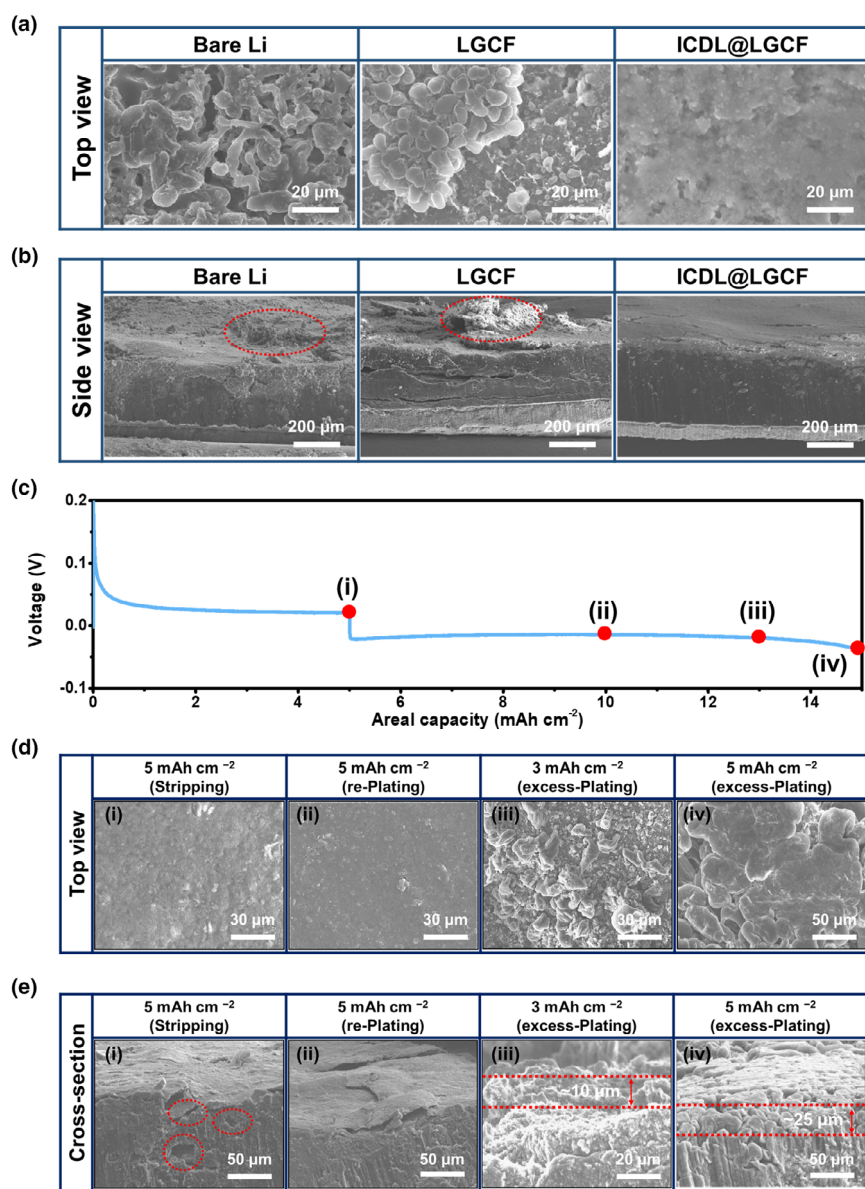
Figure 3. Ex-situ SEM images of a) top-views and b) side-views of bare Li, LGCF, and ICDL@LGCF electrodes after 100 cycles at the current density of 1 mA cm^{-2} with a capacity of 1 mAh cm^{-2}. c) Li stripping/plating voltage profile and morphology evolutions of ICDL@LGCF during Li stripping/plating: d) Top-view and e) cross-sectional SEM images of after stripping i) 5 mAh cm^{-2}, re-plating ii) 5 mAh cm^{-2}, excess-plating iii) 3 mAh cm^{-2} and iv) 5 mAh cm^{-2} at 1 mA cm^{-2}.

conducted using ex-situ SEM analysis (Figure 3c). When 5 mAh cm^{-2} of Li was stripped, Li protrusions were formed, and porous surfaces were observed on the LGCF and bare Li as shown in Figures S13a–b(i) and S14a–b(i), Supporting Information. After re-plating 5 mAh cm^{-2} of Li, both electrodes showed a rough surface with several Li dendrites, indicating irreversible Li deposition as shown in Figures S13a–b(ii) and S14a–b(ii), Supporting Information. In contrast, the morphology of the ICDL@LGCF maintained a smooth surface without any Li protrusions after stripping 5 mAh cm^{-2} of Li as shown in Figure 3d(i). Due to the high Li ion conductivity and dielectric property that form a distributed electric field provided by the ICDL, Li ions preferentially moved across the interface, leading to the stripping of the underlying Li. This result

was further supported by the cross-sectional SEM image, where empty holes (highlighted by red circles) under the ICDL were observed as shown in Figure 3e(i). Surprisingly, after re-plating 5 mAh cm^{-2} of Li, the original morphology of the surface still remained intact, and the empty holes were filled again (Figure 3d(ii),e(ii)). By observing the phenomenon of Li plating/stripping under the ICDL, we can expect the upper ICDL may prevent parasitic reactions between the underlying Li and electrolyte during cycles. After further excess Li deposition, the SEM images of LGCF and bare Li revealed severe mossy Li dendrites and an uneven surface, which resulted from an unstable SEI layer and irregular Li deposition as shown in Figure S13a–b (iii–iv), Supporting Information. These morphologies hindered Li ion migration and thus increased the possibility of Li isolations. However, as for ICDL@LGCF, the electrode surface was smooth after excess Li deposition as shown in Figure 3d(iii–iv). The granular-shaped Li was grown at 3 mAh cm^{-2} and spread to the surface with a horizontal path without the formation of Li dendrites even after reaching 5 mAh cm^{-2} of Li plating. The cross-sectional SEM images clearly exhibited the morphologies and thickness variations of excess Li deposition ranging from 3 to 5 mAh cm^{-2} on the electrode surface. In Figure 3e(iii–iv), the cross-sectional SEM images of ICDL@LGCF revealed a smooth surface with tightly packed morphologies during Li plating. On the contrary, the dendritic and needles-like morphologies of the excess metallic Li were observed during excess Li plating for LGCF and bare Li as shown in Figure S14a–b(iii–iv), Supporting Information. Furthermore, the thickness changes of excess Li deposition were measured to range from 10 to 25 μm for ICDL@LFCF, from 25 to 40 μm for LGCF, and from 30 to 60 μm for bare Li, respectively. Based on the results, the ICDL@LGCF demonstrated a uniform Li ion migration and enhanced Li ion kinetics, which led to compact and dendrite-free Li deposition on the surface, resulting in minimal volume changes. The observed morphological and structural changes supported the inhibition of Li dendrite growth and promotion of homogeneous Li deposition, facilitated by the synergetic effect of ICDL and 3D LGCF scaffold.

The surface chemical compositions of cycled electrodes were analyzed using XPS to better understand the role of ICDL in suppressing side reactions with the electrolyte and in the formation of the SEI layer (Figures S15–S19, Supporting Information). After 10 cycles of Li plating/stripping at 1 mA cm^{-2} with 1 mAh cm^{-2}, the high-resolution C 1s XPS spectra of cycled ICDL@LGCF, LGCF and bare Li revealed five significant peaks corresponding to C-C (284.8 eV), C-OR (286.3 eV), R-COOLi (288.3 eV), Li$_2$CO$_3$ (289.5 eV), and -CF (290.0 eV),

respectively (Figure S15a, Supporting Information).[69] Except for the C-C peak at 284.8 eV, the other four characteristic peaks were related to the organic SEI components and the decomposition of electrolytes.[69,70] Notably, the absence of R-COOLi, Li_2CO_3, and -CF in the cycled ICDL@LGCF demonstrated that ICDL might inhibit the parasitic reactions from the electrolyte during cycling.[63] Moreover, as shown in Figure S15b,c, Supporting Information, the high-resolution F 1s and S 2p XPS spectra further confirmed the role of ICDL in suppressing electrolyte decomposition. The peaks at 161.2, 167.9, 684.8, and 688.4 eV, corresponding to Li_xS, -TFSI, LiF, and -CF, respectively, were observed from the decomposition of Li salts in the electrolyte.[71] The significantly lower intensities of these peaks in ICDL@LGCF compared to those in LGCF and bare Li suggested that ICDL effectively suppressed the parasitic decomposition of Li salts in electrolytes.[72] The additional XPS depth profiling after 100 cycles of Li plating/stripping provided the structure and composition of the SEI layer. The XPS depth profile up to 1800 s of etching revealed that after 300 s, the signals for B and N significantly increased, indicating the presence of the ICDL layer beneath this point (Figure S16, Supporting Information). From the 0–180 s depth range, the atomic percentages of Li, N, F, S, and O were analyzed to illustrate the composition of the SEI layer (Figure S17, Supporting Information). Higher atomic percentages of F (20%) and N (2%) were detected in ICDL@LGCF compared to LGCF (F: 12%, N: 0%) and bare Li (F: 15%, N: 0%), indicating a greater presence of inorganic SEI species such as LiF and Li_3N, which are formed from the decomposition of $TFSI^-$ ions in the electrolyte. The enhanced decomposition of $TFSI^-$ ions can be attributed to the influence of the ICDL layer. The F 1s and N 1s XPS spectra of ICDL@LGCF, LGCF, and bare Li in Figure S18, Supporting Information, correspond well to the atomic percentages of F and N, as shown in Figure S17, Supporting Information. In Figure S18a, Supporting Information, ICDL@LGCF exhibits higher amounts of LiF (684.8 eV), LiN_xO_y (403.5 eV), and Li_3N (397.6 eV) in the inner SEI layer compared to LGCF and bare Li, where no Li_3N formation was observed, and the LiF content was significantly lower.[73,74] The Li 1s XPS spectra revealed organic SEI components, such as $ROCO_2Li$ (54.6 eV), on the surface of the ICDL@LGCF.[75] However, as etching progressed, the amounts of inorganic SEI species, including LiF (56 eV), Li_2CO_3 (55 eV), and Li_2O (54.2 eV), increased uniformly, with no detection of Li metal peaks.[76,77] This indicates the formation of a well-structured, compact inorganic SEI layer that effectively prevents direct contact between the Li metal and the electrolyte. The O 1s spectra presented a decrease in $ROCO_2Li$ (532.5 eV) with increasing depth, while two peaks at Li_2CO_3 (531 eV) and Li_2O (528 eV) became more prominent, supporting the existence of an organic-rich outer layer and an inorganic-rich inner layer in the SEI of ICDL@LGCF.[78] However, in Figure S18b,c, Supporting Information, the Li 1s of LGCF and bare Li shows prominent inorganic species (Li_2CO_3 and LiF) even before etching on the surface of electrodes, suggesting early decomposition of the solvent and $TFSI^-$ ion. As etching progressed, Li_2CO_3 and Li_2O became more dominant, while the amount of LiF significantly decreased. Additionally, a Li^0 (53.2 eV) peak appeared after 60 s, indicating the exposure of dendritic Li.[79] This suggested that after 100 cycles, the SEI layer on LGCF and bare Li became ruptured and less compact, resulting in a fragile and unstable SEI layer. Furthermore, the O 1s spectra showed an increase in the amount of organic-based ROLi (529.3 eV) with etching depth in LGCF and bare Li, which was more pronounced compared to ICDL@LGCF.[78] The excessive formation of Li_2O, likely from the decomposition of Li_2CO_3 at deeper etching levels, could negatively

impact the stability and performance of the SEI layer due to its poor ionic conductivity.[77,80] Additionally, Li_2CO_3 can trigger side reactions, such as gas evolution and electron tunneling, which further destabilize the SEI layer and lead to the depletion of both the electrolyte and Li metal.[77] The summary of SEI components at various etching depths, along with the Li 1s XPS spectra, is demonstrated in Figure S19, Supporting Information. In LGCF and bare Li, the SEI components were found to be heterogeneously distributed, both in the outer and inner layers. The uneven distribution of compositions resulted in a fragile and unstable SEI structure. These structural weaknesses contributed to the growth of Li dendrites due to the inhomogeneous Li ion flux. In contrast, ICDL@LGCF demonstrated a dual-layer SEI structure. The surface layer is rich in organic SEI species, while the inner layer primarily consists of inorganic SEI components, particularly LiF. This dual-layer SEI structure effectively stabilizes the SEI and enhances Li ion transport during cycling, resulting in improved stability and performance. To further investigate the uniformity of SEI layer after cycling, the cross-sectional SEM-EDS mapping of ICDL@LGCF was conducted after 100 cycles at $1\,mA\,cm^{-2}$ and $1\,mAh\,cm^{-2}$. As shown in Figure S20, Supporting Information, the N and B elements from ICDL were still homogeneously distributed on the surface, demonstrating the resilience of ICDL after multiple cycles. Additionally, the F and S elements from the SEI layer, formed after the decomposition of the electrolyte, were also detected and uniformly distributed on the surface of the electrodes.

The beneficial effect of ICDL was further studied with density functional theory (DFT). For DFT analysis, the surface models of Li_3N (001) of ICDL and LiC_6 (001) of LGCF were chosen as the substrates for investigating the adsorption energy of Li. Boron-related composites in ICDL were excluded from this analysis due to their ambiguous crystalline structure and lesser significance compared to Li_3N. **Figure 4a** shows both side and top views of the Li_3N (001) and LiC_6 (001) surfaces. The most stable adsorption sites were the top N atom for Li_3N and hollow sites of LiC_6, respectively (highlighted by red circles). The adsorption energy of Li on the Li_3N (001) surface was calculated to be -3.78 eV which was much lower than the adsorption energy (-1.44 eV) on the LiC_6 (001) surface, demonstrating that Li_3N had higher affinity to Li than LiC_6 (Figure 4b). Furthermore, we investigated the diffusion mechanism of Li in bulk Li_3N using the climbing image nudged elastic band (CI-NEB) method. The bulk Li_3N, consisting of alternating layers of Li_2N and Li, is depicted in Figure S21, Supporting Information. The possible Li diffusion pathways (Figure S22a–c, Supporting Information) were 1) from Li in a Li layer to an adjacent vacancy within the same layer (vacancy, in-plane), 2) from Li in a Li layer through the boundary of a Li_2N layer to a Li vacancy in the next layer (vacancy, through-plane), and 3) from an interstitial Li in a Li layer to an adjacent equivalent site (interstitial, in-plane). The corresponding diffusion barriers were calculated to be 1.78 eV for vacancy in-plane diffusion, 1.84 eV for vacancy through-plane diffusion, and 0.069 eV for interstitial in-plane diffusion, respectively (Figure 4c–e). The most probable Li diffusion path with the lowest barrier was the interstitial, in-plane diffusion path, which is in accordance with other theoretical calculations.[81,82] The low Li diffusion barrier contributes to excellent Li mobility of Li_3N, enhancing Li ion transport across the electrode surface and promoting a uniform Li ion flux. We further investigated the suppression of Li dendrites of Li_3N compared to LiC_6 from a thermodynamic perspective, using classical nucleation theory to explain the growth of Li dendrites.[83] The change in Gibbs free energy (ΔG) for a growing Li nucleus, assuming a spherical shape, is expressed by Equation 1, where η_n is the nucleation overpotential, $V_{m,Li}$
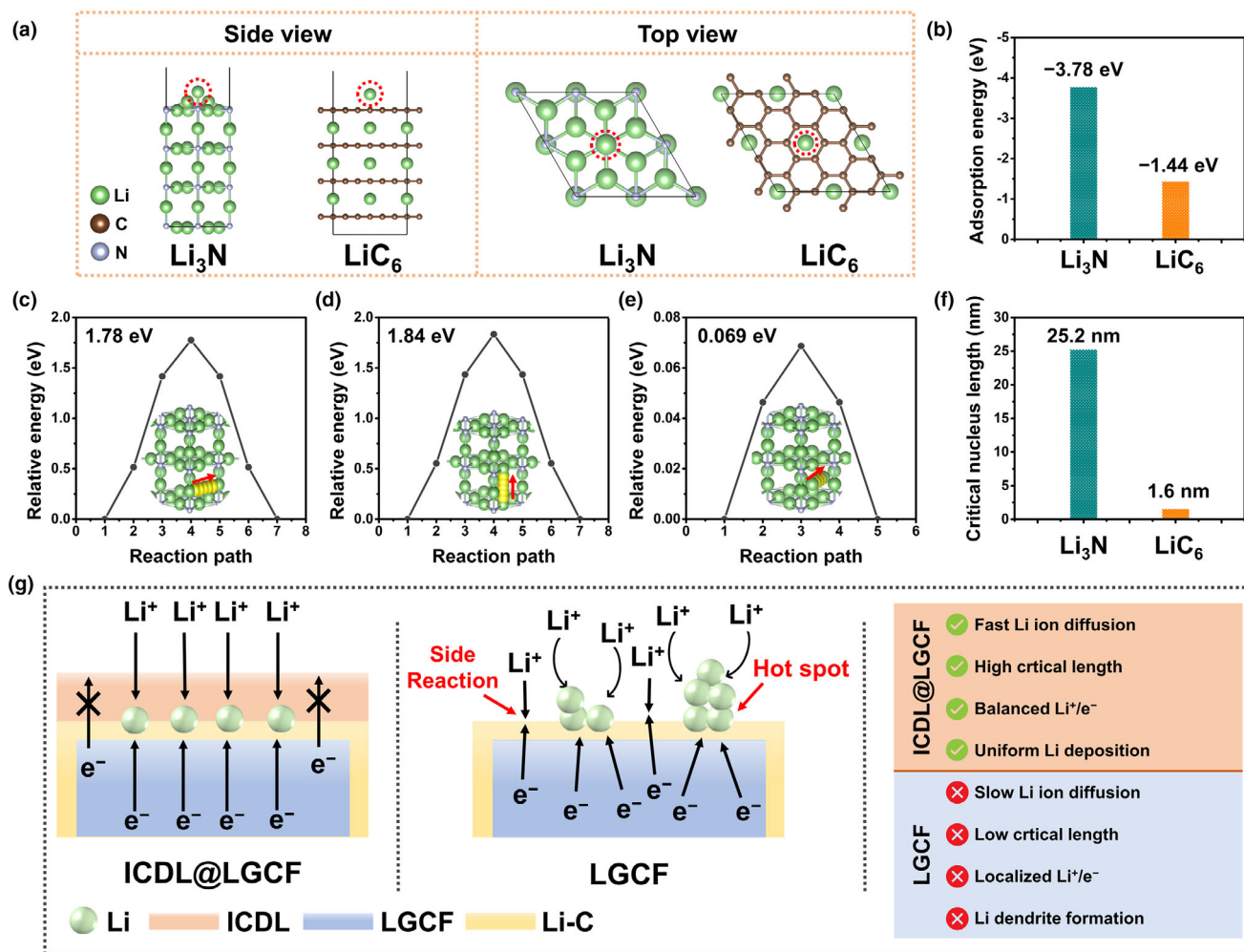
Figure 4. a) Side and top views of the Li$_3$N (001) and LiC$_6$ (001) surfaces. b) Li adsorption energy on (001) surface of Li$_3$N and LiC$_6$. The corresponding Li diffusion energy barrier of Li$_3$N at different pathways: c) along in-plane vacancy, d) through-plane vacancy, and e) in-plane interstitial Li. f) Critical nucleus length of Li on (001) surfaces of Li$_3$N and LiC$_6$. g) Schematic images of the mechanism of Li ion and electron migration during the Li deposition process of ICDL@LGCF and LGCF with a summary table highlighting the benefits of ICDL@LGCF.

is the molar volume of Li, Γ is interfacial energy between Li and substrate, r is the length of the spherical nucleus, and F is Faraday constant

$$\Delta G_{nucleation} = \Delta G_{bulk} + \Delta G_{surface} = -\frac{4F|\eta_n|\pi r^3}{3V_{m,Li}} + 4\pi\Gamma r^2 \quad (1)$$

The $\Delta G_{nucleation}$ initially increases and then decreases as ΔG_{bulk} becomes dominant with an increase in r, as shown in Figure S23, Supporting Information. The Li nucleus growth beyond the maximum $\Delta G_{nucleation}$ decreases the free energy, which induces spontaneous growth of Li dendrites. The critical length ($r_{critical}$), where $d\Delta G_{nucleation}/dr = 0$, is determined by Equation 2

$$r_{critical} = \frac{2\Gamma V_{m,Li}}{F \mid \eta_n \mid} \quad (2)$$

The $r_{critical}$ serves as a threshold that defines the energy barrier for Li nucleation and growth, and it is instrumental in evaluating the

capability to suppress the dendritic growth of Li.[84,85] By utilizing the experimental nucleation overpotential obtained from galvanostatic Li plating/stripping at $1\,mA\,cm^{-2}$, along with DFT-calculated interfacial energy between Li and the (001) substrates of Li$_3$N and LiC$_6$ (Note S1 and Table S3, Supporting Information), we calculated the $r_{critical}$ to be 25.2 and 1.6 nm for (001) surfaces of Li$_3$N and LiC$_6$, respectively (Figure 4c). Consequently, we infer that Li dendrite formation may be more effectively constrained on the Li$_3$N-rich ICDL compared to LiC$_6$, corresponding well with the SEM observations as shown in Figure 3.

According to the discussions above, the beneficial effects of the ICDL are summarized in Figure 4g. The fhBN-rich outer layer, with its dielectric properties, homogenizes the electric field and enhances Li ion flux. This uniform electric field ensures an even distribution of Li ions at the electrolyte–electrode interface, preventing localized electron accumulation and smoothly guiding the Li ions into the ICDL layer. Additionally, the outer layer suppresses electron leakage, helping to prevent side reactions. The inner layer, rich in Li$_3$N and Li-B, as shown in DFT calculations, exhibits a high critical length that suppresses Li dendrite
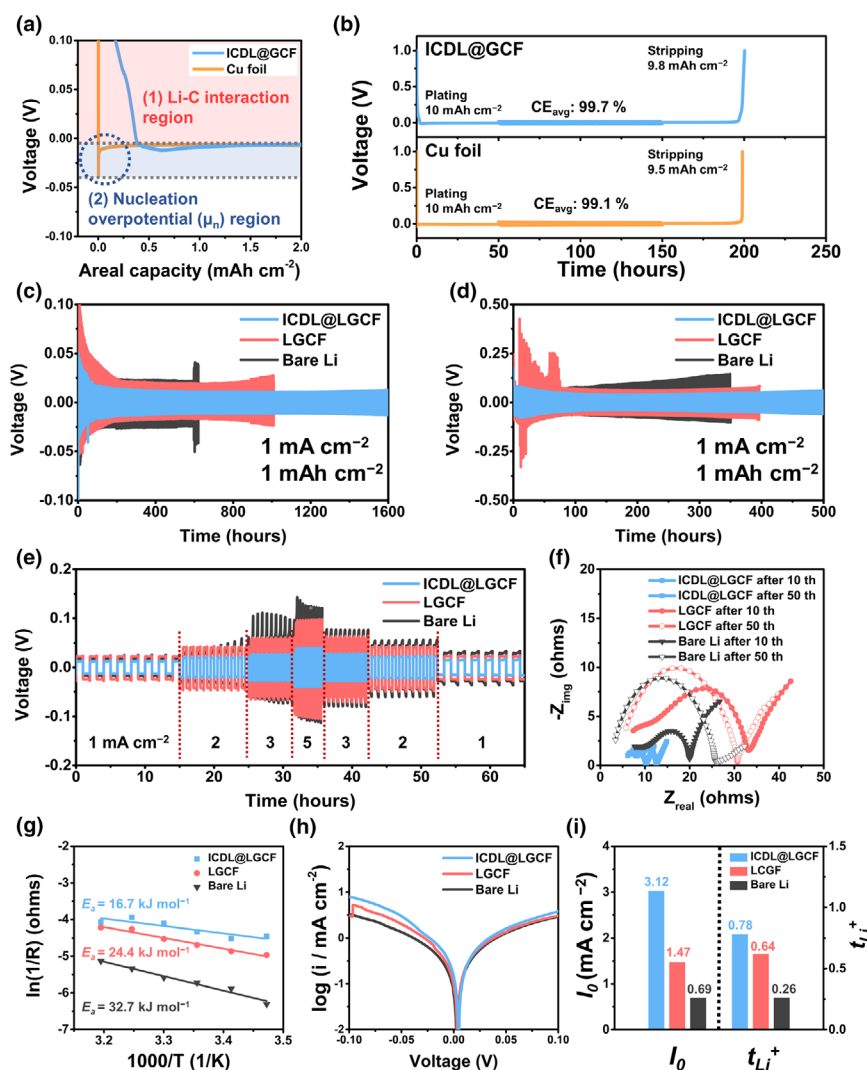
Figure 5. a) Initial voltage profile for Li plating on the ICDL@GCF and Cu foil. b) The average Coulombic efficiency (ACE) of ICDL@GCF and Cu foil at the current density of $1\,mA\,cm^{-2}$ with a capacity of $1\,mAh\,cm^{-2}$. Voltage profiles of ICDL@LGCF, LGCF, and bare Li symmetric cells at the current density of $1\,mA\,cm^{-2}$ with a capacity of $1\,mAh\,cm^{-2}$ c) in ether-based electrolyte and d) in carbonate-based electrolyte. e) Rate capability voltage profiles of symmetric cells at various current densities (1, 2, 3, and $5\,mA\,cm^{-2}$) with a fixed capacity of $1\,mAh\,cm^{-2}$ in the ether-based electrolyte. f) Nyquist plots of ICDL@LGCF, LGCF, and bare Li symmetric cells after 10 and 50 cycles at the current density of $1\,mA\,cm^{-2}$ with a capacity of $1\,mAh\,cm^{-2}$. g) Arrhenius plots for calculating activation energy (E_a) of ICDL@LGCF, LGCF, and bare Li symmetric cells. h) Tafel plots of ICDL@LGCF, LGCF, and bare Li symmetric cells obtained by CV at -0.2 to $0.2\,V$ (vs Li^+/Li) with a scan rate of $0.1\,mV\,s^{-1}$. i) Corresponding exchange current density (I_0) and Li transference number (t_{Li}^+) of ICDL@LGCF, LGCF, and bare Li symmetric cells.

formation, while enhancing Li ion conductivity, which will be further elaborated in the electrochemical analysis. This promotes rapid Li ion migration across the ICDL, supporting uniform Li plating/stripping on the underlying LGCF, while maintaining a balance between Li ions and electrons at the surface and preventing Li accumulation. In contrast, the single electron-conductive nature of LGCF, with its slower Li ion diffusion, leads to hot spots from localized Li ions and electrons at the electrode surface, resulting in Li dendrite growth. Consequently, the ICDL effectively maximizes the advantages of a 3D conductive Li host to achieve dendrite-free LMBs.

The reversibility of Li plating/stripping in the 3D Li host is a crucial factor for achieving stable battery cycling. To assess the advantages of the distinctive properties of ICDL@LGCF in promoting reversible cycling, the average Coulombic efficiency (ACE) of both ICDL@LGCF and Cu foil was measured using the Aurbach method as shown in **Figure 5**a,b.[86,87] First, pre-stripped ICDL@LGCF, referred to as ICDL@GCF, was prepared. Then, $10\,mAh\,cm^{-2}$ of Li was plated onto both the ICDL@GCF and Cu foil to conduct ACE test. The initial Li plating voltage profile of ICDL@GCF and Cu foil at $0.2\,mA\,cm^{-2}$ revealed two key regions: (1) the Li-C interaction region ranging from 1.0 to 0 V, and (2) the nucleation overpotential (μ_n) region below 0 V, which reflected the lithiophilicity of the substrate (determined by the difference between the voltage dip and the stable voltage states). The Cu foil exhibited a sharp voltage drop below 0 V, indicating no interaction between Li and the Cu substrate. In contrast, ICDL@GCF showed a smooth voltage decline, with $0.4\,mAh\,cm^{-2}$ of capacity attributed to Li-C interaction. While the $0.4\,mAh\,cm^{-2}$ of Li-C interaction could suggest some degree of irreversible Li loss, the previous literature has demonstrated the high lithiophilicity and electron conductivity of Li-C composites.[34] The lithiophilicity of Li-C was further validated in the μ_n region, where ICDL@GCF exhibited a significantly lower μ_n (6 mV) compared to Cu foil (31 mV), indicating superior lithiophilicity of the Li-C interaction and ICDL layer of the ICDL@GCF. Figure 5b presents the ACE results at $1\,mA\,cm^{-2}$ with a capacity of $1\,mAh\,cm^{-2}$ where ICDL@GCF achieved a higher ACE of 99.7% compared to 99.1% for Cu foil. The enhanced ACE of ICDL@GCF compared to Cu foil was attributed to the synergistic effects of the ICDL layer, which effectively suppressed side reactions and enhanced Li utilization during cycling.

To evaluate the cycling performances of ICDL@LGCF, LGCF, and bare Li, the galvanostatic Li plating/stripping tests were conducted using symmetric cells at different current densities and various areal capacities in an ether-based electrolyte ($1\,M$ LiTFSI in DOL/DME with 2 wt % $LiNO_3$). The cycling stability of symmetric cells was first investigated at $1\,mA\,cm^{-2}$ with a capacity of $1\,mAh\,cm^{-2}$ as shown in Figure 5c. During the initial states of symmetric cells at 200 h, ICDL@LGCF symmetric cells exhibited stable and symmetrical overpotentials as shown in Figure S25a, Supporting Information. On the other hand, the LGCF and bare Li exhibited asymmetrical voltage behavior caused by an uneven Li deposition and an unstable SEI layer formation. In addition, the Bare Li‖ Bare Li symmetric cell showed voltage fluctuation and its overpotential rose rapidly after 600 h (Figure S25b, Supporting Information),

indicating short circuits and cell failure. The LGCF‖LGCF symmetric cell displayed cycle stability up to 1000 h, attributed to the stable hosting of Li within the 3D LGCF scaffold. However, the voltage polarization gradually increased up to 30 mV after 1000 h (Figure S25c, Supporting Information). In contrast to Bare Li‖Bare Li and LGCF‖LGCF symmetric cells, the ICDL@LGCF‖ICDL@LGCF symmetric cell delivered a prolonged cycle stability up to 1600 h with low-voltage polarization (12 mV) indicating enhanced cycle stability due to the combination effects of ICDL and 3D conductive LGCF scaffold. When the current density was increased to 2 mA cm^{-2} with a fixed areal capacity at 1 mAh cm^{-2}, the ICDL@LGCF‖ICDL@LGCF achieved a long lifespan of up to 800 h (Figure S26, Supporting Information), while Bare Li‖Bare Li and LGCF‖LGCF symmetric cells exhibited a gradually increased voltage polarization and underwent sudden voltage fluctuation within 250 h. Under the more challenging condition of increased areal capacity at 2 mAh cm^{-2} with a fixed current density at 2 mA cm^{-2}, ICDL@LGCF‖ICDL@LGCF symmetric cell showed cycle stability up to 500 h with low overpotential (30 mV) as shown in Figure S27, Supporting Information. However, Bare Li‖Bare Li and LGCF‖LGCF symmetric cells were unable to maintain cycles beyond 100 h, indicating severe voltage fluctuations. The stability of LMBs in carbonate-based electrolytes is well recognized to be lower than that in ether-based electrolytes.[88] Therefore, it is meaningful to investigate the galvanostatic cycle stability of the ICDL@LGCF‖ICDL@LGCF symmetric cell in a carbonate-based electrolyte (1.3 M LiPF$_6$ in EC/DEC with 10 wt % FEC) as shown in Figure 5d. The ICDL@LGCF‖ICDL@LGCF symmetric cell also demonstrated excellent cycle performance, maintaining stability for up to 500 h with a much lower voltage hysteresis (40 mV) compared to Bare Li‖Bare Li and LGCF‖LGCF symmetric cells. These enhanced cycling performances were attributed to the uniform Li ion flux, accelerated ion transfer, and decreased volume change due to the synergistic effect of the designed ICDL and interconnected 3D conductive LGCF scaffolds. The rate performances of symmetric cells were further conducted at various current densities ranging from 1 to 5 mA cm^{-2} with a fixed capacity of 1 mAh cm^{-2} (Figure 5e). The ICDL@LGCF‖ICDL@LGCF symmetric cell delivered a stable voltage polarization under various current densities and showed low overpotential (38 mV) even at 5 mA cm^{-2}, while Bare Li‖Bare Li and LGCF‖LGCF symmetric cells delivered higher overpotential 92 and 130 mV, respectively. Upon returning to a current density of 1 mA cm^{-2}, the overpotential of ICDL@LGCF‖ICDL@LGCF symmetric cell recovered to 12 mV, indicating that ICDL@LGCF has a good rate capability even at higher current densities and excellent Li plating/stripping reversibility during the cycle.

Further electrochemical analysis was conducted to verify the superior electrochemical performance of ICDL@LGCF compared to control electrodes. At first, we measured electrochemical impedance spectroscopy (EIS) of symmetric cells to investigate the interfacial resistance during Li plating/stripping at various states. Figure S28, Supporting Information, shows equivalent circuit models for fitting Nyquist plots. The high- and medium-frequency regions in Nyquist plots reflected an interfacial resistance (R_{sei}) and a charge transfer resistance (R_{ct}) on the surfaces of Li metal, respectively. Figure S29, Supporting Information, shows the EIS results of pristine symmetric cells. The pristine ICDL@LGCF‖ICDL@LGCF symmetric cell had a lower total impedance (R_{tot}; the sum of R_{sei} and R_{ct}) than LGCF‖LGCF and Bare Li‖Bare Li symmetric cells due to the introduction of ICDL on the electrode surface (Table S1, Supporting Information). Furthermore, after 10 and 50 cycles at 1 mA cm^{-2} with a capacity of 1 mAh cm^{-2}, the R_{tot} values of

ICDL@LGCF‖ICDL@LGCF symmetric cell reduced to 6.0 and 4.4 Ω, respectively. But for the LGCF‖LGCF and Bare Li‖Bare Li symmetric cells, they exhibited significantly higher R_{tot} values which were attributed to Li dendrites formation and an unstable SEI layer on the electrodes during cycling (Figure 5f). Additionally, we calculated the diffusion coefficient (D) for cycled symmetric cells using the low-frequency region of the Nyquist plots. As shown in Figure S30, Supporting Information, the Warburg factor (σ) is determined from the linear relationship between the real impedance vs ω$^{-1/2}$ (ω = 2πf). The D value was calculated to be 8.88 × 10^{-9} cm^2 s^{-1} for ICDL@LGCF, 4.29 × 10^{-10} cm^2 s^{-1} for LGCF, and 8.15 × 10^{-10} cm^2 s^{-1} for bare Li symmetric cells.[89] The EIS and diffusion coefficient results were consistent with the symmetric cell tests and verified reduced Li ion diffusion barriers on the surface of Li metal with the introduction of ICDL. To further validate the improved Li ion kinetics in ICDL@LGCF, the temperature-dependent EIS tests were performed on symmetric cells over a ranging from 15 to 40 °C to obtain the activation energy (E_a), providing insight into improved Li ion migration through the electrode–electrolyte interface (Figure S31, Supporting Information). By fitting the data to the Arrhenius equation, we obtained activation energies of 16.7 kJ mol^{-1} for ICDL@LGCF, 24.4 kJ mol^{-1} for LGCF, and 32.7 kJ mol^{-1} for bare Li symmetric cells in Figure 5g.[90] The significantly lower E_a for ICDL@LGCF was attributed to the presence of Li$_3$N and Li-B components, which enhance Li ion conductivity and facilitate improved Li ion transport. The exchange current density (I_0) was also calculated using Tafel plots to further investigate the improved electrode kinetics via the synergetic effect of ICDL and 3D LGCF scaffolds. Figure 5h,i show the Tafel plots and I_0 values of ICDL@LGCF, LGCF, and bare Li. The I_0 values obtained by fitting the Tafel plots were 3.021 mA cm^{-2} for ICDL@LGCF, 1.47 mA cm^{-2} for LGCF, and 0.691 mA cm^{-2} for bare Li. The synergetic advantages were also confirmed by higher I_0 values of ICDL@LGCF, indicating enhanced Li plating/stripping reversibility and reduced interfacial diffusion barrier. The Li ion transference number (t_{Li}^+) was measured to evaluate the electrode capability for transporting Li ion through the electrode surface (Figure 5i and Figure S32, Supporting Information). Benefiting from the high Li ion conductivity of Li$_3$N and Li-B components in ICDL, ICDL@LGCF exhibited a significantly high t_{Li}^+ value of 0.78, compared to 0.64 and 0.26 for LGCF and bare Li, respectively.[91]

We fabricated a full cell pairing with the LiFePO$_4$ (LFP) and LiNi$_{0.8}$Co$_{0.1}$Mn$_{0.1}$O$_2$ (NCM811) as a cathode with the ICDL@LGCF, LGCF, and bare Li as anode to validate the practical application of the ICDL@LGCF. At first, we tested the cycle and rate test of full cells with a low areal mass loading LFP (5 mg cm^{-2}, N/P ratio: 35.8). **Figure 6a** exhibits the cycling performance of the LFP‖ICDL@LGCF, LFP‖LGCF, and LFP‖Bare Li full cells at 1.0 C for 500 cycles. The initial specific capacities of the LFP‖ ICDL@LGCF, LFP‖LGCF, and LFP‖Bare Li full cells at 1.0 C exhibited 127.4, 128.2, and 115.1 mAh g^{-1}, respectively. Surprisingly, LFP‖ICDL@LGCF full cell demonstrated excellent cycle stability over 500 cycles and maintained specific capacities at 117.5 mAh g^{-1} with a high capacity retention of 92.1% at 1.0 C. In contrast, LFP‖ LGCF and LFP‖Bare Li full cells showed decayed specific capacity of 94.7 and 66.5 mAh g^{-1} after 500 and 180 cycles with capacity retentions of 73.5 and 57.8%, respectively, at 1.0 C. As shown in Figure 6b, the galvanostatic charge/discharge profile of LFP‖ICDL@LGCF full cell further proved low charge/discharge voltage overpotential even after 200th cycles. The LFP‖ICDL@LGCF full cell exhibited a minimal charge/discharge voltage overpotential (0.16 V) without noticeable capacity decay. In contrast, the galvanostatic charge/discharge profile of
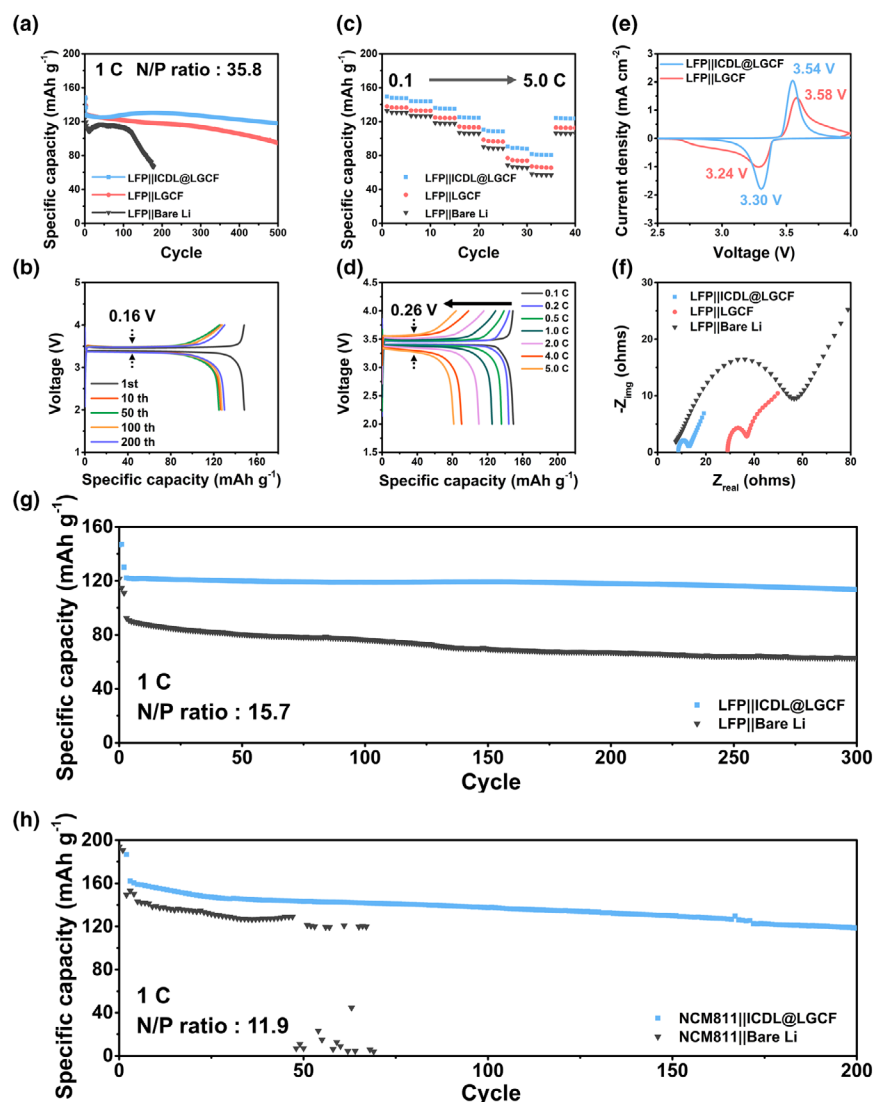
Figure 6. Electrochemical performances of full cell paired with LiFePO₄ (LFP) and LiNi₀.₈Co₀.₁Mn₀.₁O₂ (NCM811). a) Cycle performances of the low areal mass loading (5 mg cm^{-2}, N/P ratio: 35.8) LFP‖ICDL@LGCF, LFP‖LGCF, and LFP‖Bare Li full cells at 1 C. b) Galvanostatic charge/discharge profiles of LFP‖ICDL@LGCF full cell at different cycles. c) Rate performances of the LFP‖ICDL@LGCF, LFP‖LGCF, and LFP‖Bare Li full cells at 0.1, 0.2, 0.5, 1.0, 2.0, 4.0, and 5.0 C. d) Galvanostatic charge/discharge profiles of LFP‖ICDL@LGCF full cell at different C-rates. e) The CV curves of LFP‖ICDL@LGCF and LFP‖LGCF full cells at scan rate 0.1 mV s^{-1}. f) The EIS profiles of LFP‖ICDL@LGCF, LFP‖LGCF, and LFP‖Bare Li full cells after 50 cycles at 1 C. Cycle performances of the ICDL@LGCF and bare Li full cells with g) high areal mass loading LFP (12 mg cm^{-2}, N/P ratio: 15.7) and h) high areal mass loading NCM811 (10 mg cm^{-2}, N/P ratio: 11.9).

LFP‖LGCF and LFP‖Bare Li full cells showed much higher charge/discharge overpotential of 0.31 and 0.77 V at 200 th cycle, respectively. Also, much faster specific capacity decay was shown during cycle tests (Figure S33, Supporting Information). High voltage overpotential and faster specific capacity decay during cycles occurred by the growth of Li dendrites and accumulation of dead Li on the surface of LGCF and bare Li, leading to higher resistance of the cells. Table S4, Supporting Information, compares cycle stability and capacity retention of full cells in our work with previously reported works on 3D carbon-based Li hosts. Our work showed excellent cycle stability with high capacity retention. Rate performances of the LFP‖ICDL@LGCF, LFP‖LGCF, and LFP‖Bare Li full cells are also displayed in Figure 6c. The LFP‖ICDL@LGCF full cell delivered high specific capacities of 150.0, 144.3, 135.9, 125.3, 110.2, 90.6, and 81.6 mAh g^{-1} at 0.1, 0.2, 0.5, 1.0, 2.0, 4.0, and 5.0 C, respectively. These capacities were much higher than the specific capacities of LFP‖LGCF and LFP‖Bare Li full cells, indicating excellent electrochemical kinetics of ICDL@LGCF. Figure 6d further displays the galvanostatic charge/discharge profile of LFP‖ICDL@LGCF full cell at different rates. The charge/discharge voltage overpotentials exhibited a slow increase up to 5 C, with the overpotential of 0.26 V at 5 C for the LFP‖ICDL@LGCF full cell. In contrast, the voltage overpotentials of LFP‖LGCF and LFP‖Bare Li full cells increased rapidly with overpotentials of 0.52 and 0.55 V at 5 C, respectively (Figure S34, Supporting Information). Figure 6e exhibits cyclic voltammetry (CV) of LFP‖ICDL@LGCF and LFP‖LGCF full cells at potential range of 2.0–4.0 V (vs Li$^+$/Li) with a scan rate 0.1 mV s^{-1}. The CV of LFP‖ICDL@LGCF full cell showed a pair of redox peaks at 3.30 and 3.54 V, while a pair of redox peaks of LFP‖LGCF full cell were located at 3.28 and 3.58 V. The stronger redox peak intensity and small voltage gaps between redox pairs indicated a faster Li ion transport kinetics and smaller voltage overpotential. Furthermore, EIS results of pristine and after 50 cycles of full cells at 1 C were analyzed for underlying reasons for the smaller voltage overpotentials as shown in Figure S35, Supporting Information and Figure 6f. Both pristine and after 50 cycled full cells, the interfacial impedance of LFP‖ICDL@LGCF full cell was the lowest among other full cells. This could be attributed to the introduction of ICDL, which not only effectively distributed the electric field and Li ion flux but also facilitated fast Li ion transport across the electrode/electrolyte interface. In addition, the 3D conductive LGCF accommodating Li in the scaffold enabled to mitigate severe volume changes during cycling.

Even with the high areal mass loading of LFP (12 mg cm^{-2}, N/P ratio: 15.7), further full cell tests were conducted to investigate the cycle stability of LFP‖ICDL@LGCF and LFP‖Bare Li full cells, aiming to demonstrate their practical application for LMBs under more harsh conditions. In Figure 6h, LFP‖ICDL@LGCF full cell demonstrates an initial specific capacity of 122.2 mAh g^{-1} at 1.0 C and exhibited stable cycle performance over 300 cycles without noticeable decay (capacity retention 93.4%), while LFP‖Bare Li full cell exhibited a lower specific capacity (88.7 mAh g^{-1}) at 1.0 C and experienced severe capacity degradation (capacity retention 67.3%) during cycling. Furthermore, the galvanostatic charge/discharge profiles of ICDL@LGCF exhibited lower voltage overpotential (0.25 V) than that of LFP‖Bare Li (0.48 V) after 300 cycles

(Figure S36, Supporting Information). Similarly, the ICDL@LGCF continued to present excellent cycle performance when paired with high areal mass loading NCM811 (10 mg cm^{-2}, N/P ratio: 11.9) as a cathode in the full cell. Figure 6i demonstrates that the NCM811‖ICDL@LGCF delivered 130.1 mAh g^{-1} at 1 C after 150 cycles with a capacity retention of 81.3%. On the contrary, NCM811‖Bare Li exhibited severe capacity degradation and fluctuations after 50 cycles. The charge/discharge profile comparisons, as shown in Figure S37, Supporting Information, highlight the stable voltage hysteresis in the NCM811‖ICDL@LGCF throughout the cycles. In contrast, the NCM811‖Bare Li displayed severe voltage fluctuations and short-circuit behavior at the 50th cycle. To evaluate cycling performance at a lower N/P ratio (Figure S38, Supporting Information), we prepared an ICDL@LGCF electrode with 5 mAh cm^{-2} of Li plating and paired it with an LFP cathode (2.5 mAh cm^{-2}), achieving an N/P ratio of 2. The LFP‖ICDL@LGCF full cell showed stable performance during 50 cycles, maintaining a specific capacity of 125 mAh g^{-1} and a Coulombic efficiency of 99% at 0.5 C. These results confirmed that the synergetic effect of innovative characteristics of the ICDL and the 3D conductive LGCF has made ICDL@LGCF electrode an outstanding LMAs for Li metal batteries.

3. Conclusion

To conclude, we proposed a Li ionic conductive-dielectric gradient bifunctional interlayer (denoted as ICDL) to the 3D Li-injected graphene/carbon nanotube scaffold (LGCF) by a simple vacuum filtration and molten Li injection process. By controlling the layer structure, the ICDL layer consists of an outer fhBN-rich layer and an inner layer abundant in Li$_3$N and Li-B, facilitating high Li ion conductivity and superior dielectric properties. The synergistic effects of the ICDL ensure uniform Li ion distribution and promote electron transport kinetics without the formation of hot spots, as verified by electrochemical analyses and theoretical calculations. As a result, the ICDL@LGCF demonstrates a remarkable cycling stability, presenting 1600 h with minimal voltage hysteresis within 15 mV at 1 mA cm^{-2} and 1 mAh cm^{-2}. Additionally, when integrated into full cells with LiFePO$_4$ (LFP), it exhibits good cycle stability and substantial capacity retention of 93.4% after 300 cycles at 1 C. When paired with LiNi$_{0.8}$Co$_{0.1}$Mn$_{0.1}$O$_2$ (NCM811) cathode, ICDL@LGCF full cells demonstrate a better cycle stability compared with bare Li over 200 cycles. This work validates the integration of a bifunctional interlayer to optimize the 3D conductive scaffold for Li hosting, thereby advancing the practical application of Li metal anodes.

4. Experimental Section

Detailed information related to the synthesis of active electrodes, physicochemical characterization, and electrochemical evaluation of bifunctional electrodes towards UOR and supercapacitor application is provided in Supporting Information.

Conflict of Interest

The authors declare no conflict of interest.

Supporting Information

Supporting Information is available from the Wiley Online Library or from the author.

[1] D. Lin, Y. Liu, Y. Cui, *Nat. Nanotechnol.* **2017**, *12*, 194.
[2] W. Xu, J. Wang, F. Ding, X. Chen, E. Nasybulin, Y. Zhang, J. G. Zhang, *Energy Environ. Sci.* **2014**, *7*, 513.
[3] J. Janek, W. G. Zeier, *Nat. Energy* **2016**, *1*, 16141.
[4] Y. Zhang, T. T. Zuo, J. Popovic, K. Lim, Y. X. Yin, J. Maier, Y. G. Guo, *Mater. Today* **2020**, *33*, 56.
[5] Z. Hu, S. Zhang, S. Dong, Q. Li, G. Cui, L. Chen, *Chem. Mater.* **2018**, *30*, 4039.
[6] L. Chen, X. Fan, X. Ji, J. Chen, S. Hou, C. Wang, *Joule* **2019**, *3*, 732.
[7] Y. Guo, H. Li, T. Zhai, *Adv. Mater.* **2017**, *29*, 1700007.
[8] G. Wang, X. Xiong, D. Xie, X. Fu, X. Ma, Y. Li, Y. Liu, Z. Lin, C. Yang, M. Liu, *Energy Storage Mater.* **2019**, *23*, 701.
[9] C. Yan, X. B. Cheng, Y. X. Yao, X. Shen, B. Q. Li, W. J. Li, R. Zhang, J. Q. Huang, H. Li, Q. Zhang, *Adv. Mater.* **2018**, *30*, 1804461.
[10] G. Bieker, M. Winter, P. Bieker, *Phys. Chem. Chem. Phys.* **2015**, *17*, 8670.
[11] X. Shen, R. Zhang, X. Chen, X. B. Cheng, X. Li, Q. Zhang, *Adv. Energy Mater.* **2020**, *10*, 1903645.
[12] H. Kim, Y. J. Gong, J. Yoo, Y. S. Kim, *J. Mater. Chem. A* **2018**, *6*, 15540.
[13] J. Zhu, P. Li, X. Chen, D. Legut, Y. Fan, R. Zhang, Y. Lu, X. Cheng, Q. Zhang, *Energy Storage Mater.* **2019**, *16*, 426.
[14] N. W. Li, Y. X. Yin, J. Y. Li, C. H. Zhang, Y. G. Guo, *Adv. Sci.* **2017**, *4*, 1600400.
[15] X. Li, J. Zheng, X. Ren, M. H. Engelhard, W. Zhao, Q. Li, J. G. Zhang, W. Xu, *Adv. Energy Mater.* **2018**, *8*, 1703022.
[16] Y. Ma, Z. Zhou, C. Li, L. Wang, Y. Wang, X. Cheng, P. Zuo, C. Du, H. Huo, Y. Gao, G. Yin, *Energy Storage Mater.* **2018**, *11*, 197.
[17] N. Piao, S. Liu, B. Zhang, X. Ji, X. Fan, L. Wang, P. F. Wang, T. Jin, S. C. Liou, H. Yang, J. Jiang, K. Xu, M. A. Schroeder, X. He, C. Wang, *ACS Energy Lett.* **2021**, *6*, 1839.
[18] D. Wang, H. Liu, M. Li, D. Xia, J. Holoubek, Z. Deng, M. Yu, J. Tian, Z. Shan, S. P. Ong, P. Liu, Z. Chen, *Nano Energy* **2020**, *75*, 104889.
[19] X. Shangguan, G. Xu, Z. Cui, Q. Wang, X. Du, K. Chen, S. Huang, G. Jia, F. Li, X. Wang, D. Lu, S. Dong, G. Cui, *Small* **2019**, *15*, 1900269.
[20] X. Fan, X. Ji, F. Han, J. Yue, J. Chen, L. Chen, T. Deng, J. Jiang, C. Wang, *Sci. Adv.* **2018**, *4*, eaau9245.
[21] X. Q. Zhang, T. Li, B. Q. Li, R. Zhang, P. Shi, C. Yan, J. Q. Huang, Q. Zhang, *Angew. Chem. Int. Ed.* **2020**, *59*, 3252.

[22] H. Duan, Y. X. Yin, Y. Shi, P. F. Wang, X. D. Zhang, C. P. Yang, J. L. Shi, R. Wen, Y. G. Guo, L. J. Wan, *J. Am. Chem. Soc.* **2018**, *140*, 82.

[23] S. H. Lee, J. Y. Hwang, J. Ming, H. Kim, H. G. Jung, Y. K. Sun, *ACS Energy Lett.* **2021**, *6*, 2153.

[24] C. Z. Zhao, B. C. Zhao, C. Yan, X. Q. Zhang, J. Q. Huang, Y. Mo, X. Xu, H. Li, Q. Zhang, *Energy Storage Mater.* **2020**, *24*, 75.

[25] M. Bae, Y. Kim, J. Choi, S. Park, L. Lin, T. Yoo, H. Hong, D. Jung, Y. Piao, *Carbon* **2022**, *196*, 663.

[26] S. S. Chi, Y. Liu, W. L. Song, L. Z. Fan, Q. Zhang, *Adv. Funct. Mater.* **2017**, *27*, 1700348.

[27] Y. Lv, Q. Zhang, C. Li, C. Ma, W. Guan, X. Liu, Y. Ding, *ACS Sustain. Chem. Eng.* **2022**, *10*, 7188.

[28] W. Song, S. Cui, J. Zhang, S. Fan, L. Chen, H. M. Zhang, Y. Zhang, X. Meng, *ACS Appl. Mater. Interfaces* **2023**, *15*, 9421.

[29] H. Qiu, T. Tang, M. Asif, X. Huang, Y. Hou, *Adv. Funct. Mater.* **2019**, *29*, 1808468.

[30] Y. Zhao, Q. Sun, X. Li, C. Wang, Y. Sun, K. R. Adair, R. Li, X. Sun, *Nano Energy* **2018**, *43*, 368.

[31] Q. Chen, Y. Wei, X. Zhang, Z. Yang, F. Wang, W. Liu, J. Zuo, X. Gu, Y. Yao, X. Wang, *Adv. Energy Mater.* **2022**, *12*, 2200072.

[32] Y. H. Kim, G. W. Lee, Y. J. Choi, H. S. Choi, K. B. Kim, *Adv. Funct. Mater.* **2022**, *32*, 2113316.

[33] D. J. Yoo, S. Choi, Y. Cho, J. Kim, S. J. Lee, S. H. Choi, T. W. Kwon, K. Char, K. J. Kim, A. Coskun, J. W. Choi, *Adv. Mater.* **2019**, *31*, 1901645.

[34] D. Lin, Y. Liu, Z. Liang, H. W. Lee, J. Sun, H. Wang, K. Yan, J. Xie, Y. Cui, *Nat. Nanotechnol.* **2016**, *11*, 626.

[35] G. Huang, J. Han, F. Zhang, Z. Wang, H. Kashani, K. Watanabe, M. Chen, *Adv. Mater.* **2019**, *31*, 1805334.

[36] L. Enze, *J. Phys. D. Appl. Phys.* **1987**, *20*, 1609.

[37] M. Bae, S. J. Park, M. Kim, E. Kwon, S. Yu, J. Choi, Y. Chang, Y. Kim, Y. J. Choi, H. Hong, L. Lin, W. Zhang, S. Park, J. Y. Maeng, J. Park, S. Y. Lee, S. H. Yu, Y. Piao, *Adv. Energy Mater.* **2024**, *14*, 2304101.

[38] Y. He, Y. Zhang, H. M. K. Sari, Z. Wang, Z. Lü, X. Huang, Z. Liu, J. Zhang, X. Li, *Nano Energy* **2021**, *89*, 106334.

[39] Y. Zhang, M. Yao, T. Wang, H. Wu, Y. Zhang, *Angew. Chem. Int. Ed.* **2024**, *63*, e202403399.

[40] T. Yu, T. Zhao, N. Zhang, T. Xue, Y. Chen, Y. Ye, F. Wu, R. Chen, *Nano Lett.* **2023**, *23*, 276.

[41] C. Wang, M. Liu, M. Thijs, F. G. Ooms, S. Ganapathy, M. Wagemaker, *Nat. Commun.* **2021**, *12*, 6536.

[42] M. Ye, X. Jin, X. Nan, J. Gao, L. Qu, *Energy Storage Mater.* **2020**, *24*, 153.

[43] K. K. Kim, A. Hsu, X. Jia, S. M. Kim, Y. Shi, M. Dresselhaus, T. Palacios, J. Kong, *ACS Nano* **2012**, *6*, 8583.

[44] Z. Wang, S. Qin, F. Chen, S. Chen, D. Liu, D. Jiang, P. Zhang, P. Mota Santiago, D. Hegh, P. Lynch, *ACS Nano* **2024**, *18*, 3531.

[45] J. Wu, X. Li, Z. Rao, X. Xu, Z. Cheng, Y. Liao, L. Yuan, X. Xie, Z. Li, Y. Huang, *Nano Energy* **2020**, *72*, 104725.

[46] Y. Luo, T. Li, H. Zhang, W. Liu, X. Zhang, J. Yan, H. Zhang, X. Li, *Angew. Chem. Int. Ed.* **2021**, *60*, 11718.

[47] M. Li, X. Yang, D. Wu, Q. Zhang, X. Wei, Y. Cheng, M. D. Gu, *ACS Appl. Mater. Interfaces* **2023**, DOI: 10.1021/acsami.3c11673.

[48] M. R. Shaik, M. Bissannagari, Y. M. Kwon, K. Y. Cho, J. Kim, S. Yoon, *J. Chem. Eng.* **2021**, *424*, 130326.

[49] X. An, Y. Liu, K. Yang, J. Mi, J. Ma, D. Zhang, L. Chen, X. Liu, S. Guo, Y. Li, Y. Ma, M. Liu, Y. B. He, F. Kang, *Adv. Mater.* **2024**, *36*, 2311195.

[50] J. Wen, Y. Huang, J. Duan, Y. Wu, W. Luo, L. Zhou, C. Hu, L. Huang, X. Zheng, W. Yang, Z. Wen, Y. Huang, *ACS Nano* **2019**, *13*, 14549.

[51] Y. Huang, B. Chen, J. Duan, F. Yang, T. Wang, Z. Wang, W. Yang, C. Hu, W. Luo, Y. Huang, *Angew. Chem. Int. Ed.* **2020**, *59*, 3699.

[52] E. K. Jang, J. Ahn, S. Yoon, K. Y. Cho, *Adv. Funct. Mater.* **2019**, *29*, 1905078.

[53] Y. Liu, C. Sun, Y. Lu, X. Lin, M. Chen, Y. Xie, C. Lai, W. Yan, *J. Chem. Eng.* **2023**, *451*, 138570.

[54] X. L. Li, S. Huang, D. Yan, J. Zhang, D. Fang, Y. V. Lim, Y. Wang, T. C. Li, Y. Li, L. Guo, H. Y. Yang, *Energy Environ. Mater.* **2023**, *6*, e12274.

[55] K. Zhu, P. Xue, G. Cheng, M. Wang, H. Wang, C. Bao, K. Zhang, Q. Li, J. Sun, S. Guo, Y. Yao, C. P. Wong, *Energy Storage Mater.* **2021**, *43*, 130.

[56] Q. Cheng, A. Li, N. Li, S. Li, A. Zangiabadi, T.-D. Li, W. Huang, A. C. Li, T. Jin, Q. Song, W. Xu, N. Ni, H. Zhai, M. Dontigny, K. Zaghib, X. Chuan, D. Su, K. Yan, Y. Yang, *Joule* **2019**, *3*, 1510.

[57] J. Cai, W. Jolie, C. C. Silva, M. Petrović, C. Schlueter, T. Michely, M. Kralj, T. L. Lee, C. Busse, *Phys. Rev. B* **2018**, *98*, 195443.

[58] P. R. Kidambi, R. Blume, J. Kling, J. B. Wagner, C. Baehtz, R. S. Weatherup, R. Schloegl, B. C. Bayer, S. Hofmann, *Chem. Mater.* **2014**, *26*, 6380.

[59] S. Xia, X. Zhang, L. Luo, Y. Pang, J. Yang, Y. Huang, S. Zheng, *Small* **2021**, *17*, 2006002.

[60] P. Shi, T. Li, R. Zhang, X. Shen, X. B. Cheng, R. Xu, J. Q. Huang, X. R. Chen, H. Liu, Q. Zhang, *Adv. Mater.* **2019**, *31*, 1807131.

[61] M. Wan, X. Duan, H. Cui, J. Du, L. Fu, Z. Chen, Z. Lu, G. Li, Y. Li, E. Mao, L. Wang, Y. Sun, *Energy Storage Mater.* **2022**, *46*, 563.

[62] C. Chen, Q. Liang, G. Wang, D. Liu, X. Xiong, *Adv. Funct. Mater.* **2022**, *32*, 2107249.

[63] W. Cao, W. Chen, M. Lu, C. Zhang, D. Tian, L. Wang, F. Yu, *J. Energy Chem.* **2023**, *76*, 648.

[64] S. Huang, K. Long, Y. Chen, T. Naren, P. Qing, X. Ji, W. Wei, Z. Wu, L. Chen, *Nanomicro Lett.* **2023**, *15*, 235.

[65] X. D. Li, Y. M. Zhao, Y. F. Tian, Z. Y. Lu, M. Fan, X. S. Zhang, H. Tian, Q. Xu, H. L. Li, Y. G. Guo, *ACS Appl. Mater. Interfaces* **2022**, *14*, 27854.

[66] J. Xie, L. Liao, Y. Gong, Y. Li, F. Shi, A. Pei, J. Sun, R. Zhang, B. Kong, R. Subbaraman, *Sci. Adv.* **2017**, *3*, eaao3170.

[67] F. Zhu, Z. Zhang, J. Gu, J. Xu, S. Eitssayeam, Q. Xu, P. Shi, Y. Min, J. Colloid, *Interface Sci.* **2023**, *650*, 622.

[68] Y. H. Tan, Z. Liu, J.-H. Zheng, Z. J. Ju, X. Y. He, W. Hao, Y. C. Wu, W. S. Xu, H. J. Zhang, G. Q. Li, L. S. Zhou, F. Zhou, X. Tao, H. B. Yao, Z. Liang, *Adv. Mater.* **2024**, *36*, 2404815.

[69] C. Lu, M. Tian, X. Zheng, C. Wei, M. H. Rummeli, P. Strasser, R. Yang, *J. Chem. Eng.* **2022**, *430*, 132722.

[70] S. Li, X. S. Wang, Q. D. Li, Q. Liu, P. R. Shi, J. Yu, W. Lv, F. Kang, Y. B. He, Q. H. Yang, *J. Mater. Chem. A* **2021**, *9*, 7667.

[71] S. Xia, F. Li, X. Zhang, L. Luo, Y. Zhang, T. Yuan, Y. Pang, J. Yang, W. Liu, Z. Guo, *ACS Nano* **2023**, *17*, 20689.

[72] Y. Zhao, D. Wang, Y. Gao, T. Chen, Q. Huang, D. Wang, *Nano Energy* **2019**, *64*, 103893.

[73] H. Zhang, J. Ju, S. Xia, D. Sun, X. Yu, *Adv. Funct. Mater.* **2021**, *31*, 2009712.

[74] C. Chen, Q. Zhou, X. Li, B. Zhao, Y. Chen, X. Xiong, *Small Methods* **2024**, *8*, 2300839.

[75] C. Yan, X. B. Cheng, Y. Tian, X. Chen, X. Q. Zhang, W. J. Li, J. Q. Huang, Q. Zhang, *Adv. Mater.* **2018**, *30*, 1707629.

[76] D. Wu, J. He, J. Liu, M. Wu, S. Qi, H. Wang, J. Huang, F. Li, D. Tang, J. Ma, *Adv. Energy Mater.* **2022**, *12*, 2200337.

[77] Y. Guo, S. Pan, X. Yi, S. Chi, X. Yin, C. Geng, Q. Yin, Q. Zhan, Z. Zhao, F.-M. Jin, H. Fang, Y. B. He, F. Kang, S. Wu, Q. H. Yang, *Adv. Mater.* **2024**, *36*, 2308493.

[78] D. Kang, S. Sardar, R. Zhang, H. Noam, J. Chen, L. Ma, W. Liang, C. Shi, J. P. Lemmon, *Energy Storage Mater.* **2020**, *27*, 69.

[79] D. Han, Z. Wang, S. Chen, J. Zhou, S. Chen, M. Wang, D. Wu, X. Meng, C. W. Bielawski, J. Geng, *Small* **2024**, DOI: 10.1002/smll.202405453.

[80] H. Song, J. Lee, M. Sagong, J. Jeon, Y. Han, J. Kim, H. G. Jung, J.-S. Yu, J. Lee, I.-D. Kim, *Adv. Mater.* **2024**, DOI: 10.1002/adma.202407381.

[81] J. Sarnthein, K. Schwarz, P. Blöchl, *Phys. Rev. B* **1996**, *53*, 9084.

[82] W. Li, G. Wu, C. M. Araújo, R. H. Scheicher, A. Blomqvist, R. Ahuja, Z. Xiong, Y. Feng, P. Chen, *Energy Environ. Sci.* **2010**, *3*, 1524.

[83] W. Plieth, *Electrochemistry for Materials Science*, 1st Edition, Elsevier, Amsterdam; Oxford **2008**.

[84] A. Pei, G. Zheng, F. Shi, Y. Li, Y. Cui, *Nano Lett.* **2017**, *17*, 1132.

[85] J. Lopez, A. Pei, J. Y. Oh, G. N. Wang, Y. Cui, Z. Bao, *J. Am. Chem. Soc.* **2018**, *140*, 11735.

[86] S. Xia, C. Li, J. A. Yuwono, Y. Wang, C. Wang, X. Zhang, J. Yang, J. Mao, S. Zheng, Z. Guo, *Angew. Chem. Int. Ed.* **2024**, *63*, e202409327.

[87] L. Lin, L. Suo, Y. s. Hu, H. Li, X. Huang, L. Chen, *Adv. Energy Mater.* **2021**, *11*, 2003709.

[88] Y. Li, M. Liu, K. Wang, C. Li, Y. Lu, A. Choudhary, T. Ottley, D. Bedrov, L. Xing, W. Li, *Adv. Energy Mater.* **2023**, *13*, 2300918.

[89] G. W. Lee, Y. J. Choi, Y. H. Kim, S. g. Choi, H. S. Choi, H. K. Kim, K. B. Kim, *Carbon* **2022**, *198*, 289.

[90] Z. Luo, S. Li, L. Yang, Y. Tian, L. Xu, G. Zou, H. Hou, W. Wei, L. Chen, X. Ji, *Nano Energy* **2021**, *87*, 106212.

[91] H. Xu, Y. He, Z. Zhang, J. Shi, P. Liu, Z. Tian, K. Luo, X. Zhang, S. Liang, Z. Liu, *J. Energy Chem.* **2020**, *48*, 375.